https://doi.org/10.5194/essd-2026-134
Preprint. Discussion started: 20 April 2026

Open Access Earth System Science Data Discussions

RAAVEN data processing for TORUS and TORUS-LItE

Adam L. Houston[1], Mark De Bruin[1], Céu Gómez-Faulk[2], Brian Argrow[2]

[1] Department of Earth and Atmospheric Sciences, University of Nebraska-Lincoln, Lincoln, NE, 68588, USA
[2] Ann and H. J. Smead Aerospace Engineering Sciences, University of Colorado Boulder, Boulder, CO, 80303, USA

Correspondence to: Adam L. Houston (ahouston2@unl.edu)

Abstract. RAAVEN (Robust Autonomous Airborne Vehicle - Endurant and Nimble) uncrewed aircraft systems (UAS) were deployed in and around supercell thunderstorms during the Targeted Observation by Radars and UAS of Supercells (TORUS) and TORUS Left Flank Intensive Experiment (TORUS-LItE) field campaigns. On-board sensors measured temperature, humidity, pressure, and wind. Despite extensive predeployment testing, the demanding environments where data collection occurred presented numerous challenges to data quality. In this article, extensive quality control procedures adopted for these data are described. Many of these procedures aim to quantify data-quality uncertainty, in lieu of correcting questionable data. Procedures address the dependency of estimated wind on aircraft manoeuvring, periodically faulty sensors, questionable data induced by sensor wetting in rain, and sensor hysteresis and bias. Bulk data statistics are also presented, in part to assert data quality but also to highlight unique qualities of UAS data collected during TORUS and TORUS-LItE.

1 Overview

Uncrewed aircraft systems (UAS) are uniquely capable of controlled data collection in environments too hazardous for crewed aircraft. Their application towards in situ data collection for severe storms research dates back to the Port Hedland trial in Australia (Holland et al., 2001) in the late 20th century but accelerated in the US following efforts documented by Elston et al. (2011), Houston et al. (2012), and Frew et al. (2012). More recently, the RAAVEN (Robust Autonomous Airborne Vehicle - Endurant and Nimble) fixed-wing UAS has been used for in situ data collection in and around supercell thunderstorms as part of the Targeted Observation by Radars and UAS of Supercells (TORUS) and TORUS Left Flank Intensive Experiment (TORUS-LItE) field campaigns (Houston et al., 2026).

TORUS (2019 and 2022) and TORUS-LItE (2023) aimed to explicate the role of storm-generated airmass boundaries and other coherent (O(1000s)) features in the development of near-surface rotation. In TORUS-2019 and TORUS-LItE, UAS were used along with three mobile ground-based weather radars, an airborne radar, ground-based and airborne lidars, up to 10 mobile mesonet vehicles, and multiple balloon-borne sondes[1]. TORUS and TORUS-LItE (hereafter collectively referred to as TORUS) were collaborative efforts involving more than 200 scientists and engineers from the University of Nebraska-

[1] UAS were not active during the 2022 TORUS field season.

https://doi.org/10.5194/essd-2026-134
Preprint. Discussion started: 20 April 2026

Lincoln, the University of Colorado Boulder, Texas Tech University, the National Oceanic and Atmospheric Administration's National Severe Storms Laboratory, and the University of Oklahoma.

In this article we describe the extensive quality control procedures adopted for the RAAVEN data collected during TORUS. RAAVEN data have been described previously by De Boer et al. (2022b) for ATOMIC (Atlantic Tradewind Ocean–Atmosphere Mesoscale Interaction Campaign), Cleary et al. (2022) for WiscoDISCO-2021 (Wisconsin's Dynamic Influence of Shoreline Circulations on Ozone, and Lappin et al. (2024) for TRACER (TRacking Aerosol Convection interactions ExpeRiment). Nevertheless, the demanding environments where data collection occurred during TORUS presented numerous challenges to data quality that are addressed herein.

2 The RAAVEN

The RAAVEN (Figure 1) is a fixed-wing UAS designed and maintained by the University of Colorado Boulder. The airframe is custom built by RiteWing RC based on their commercially-available DRAK design. It is constructed principally of expanded polypropylene foam and has nominal take off weight of 6.8 kg. It is powered by an 8S 21000 mAh lithium-ion battery pack. In 2019 the RAAVEN was controlled by a Pixhawk 2 autopilot, that was renamed the Cube Black autopilot by CubePilot Global Pty Ltd prior to the 2023 field campaign.

Meteorological sensors onboard the RAAVEN during TORUS measured temperature, humidity, pressure, and wind. Sensor configurations for temperature and humidity differed slightly between 2019 and 2023. In 2023, two Vaisala RSS421 sensor sets were included on all RAAVEN platforms to enable fast response measurements in the free stream just above the aircraft fuselage and a shielded iPTH sensor set, including an InterMet Systems bead thermistor and IST HYT271 relative humidity sensor, was added to the side of the nose of all aircraft operating in the left-flank mission (more details on mission areas can be found in Section 3). In 2019, temperature and humidity were measured with an E+E EE03 sensor integrated into the Blackswift Technologies multi-hole probe (MHP, principally used for derivation of wind velocity). Specifications for all sensors can be found in Table 1.

3 RAAVEN TORUS Deployments

During TORUS-2019 and TORUS-LItE, coordinated deployments were conducted on 30 supercells, 11 of which were tornadic. Of these 30 supercells, UAS were deployed on all but one and were deployed on all tornadic supercells. Operations occurred in May and June of each year over a domain spanning the central US (Figure 2) where the highest probability of supercells exists in the late spring and early summer. UAS flights were conducted under nine separate Certificates of Authorization or Waivers (COAs) granted to the University of Colorado Boulder by the Federal Aviation Administration. The maximum operational flight ceiling was 760 m AGL but was restricted to 300 m near approaches to Denver International Airport (points within the region bounded by the dotted line in Figure 2).

https://doi.org/10.5194/essd-2026-134
Preprint. Discussion started: 20 April 2026

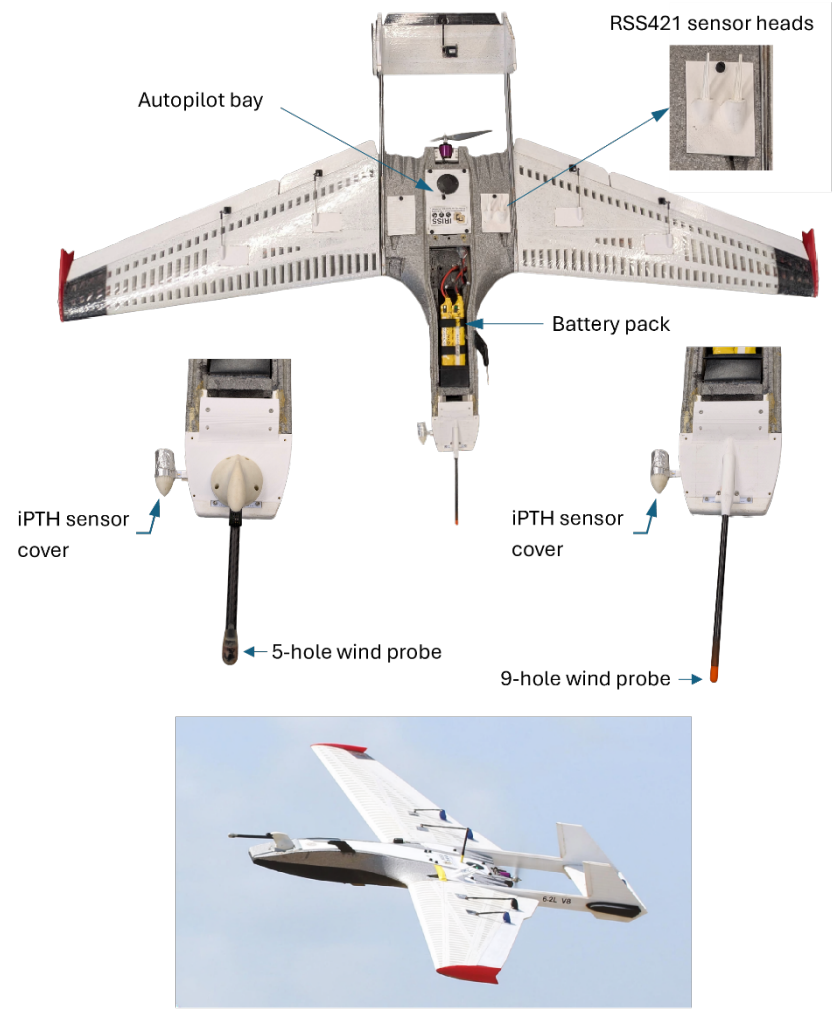

Figure 1: RAAVEN. The RAAVEN uncrewed aircraft showing locations of the two Vaisala RSS421 sensors and the shielded InterMet (iPTH) sensors. The two multi-hole probe (MHP) wind data sensors are shown with the original 5-hole MHP on the left and the updated 9-hole MHP on the right. The bottom image shows a RAAVEN in flight.

The TORUS concept of operations was structured around four mission areas defined according to their storm-relative locations (Figure 3): 1) the "left flank", located left of the low-level mesocyclone relative to the storm motion vector and within 5-10 km of the low-level mesocyclone, 2) the "right flank", located right of the mesocyclone, 3) the "near-inflow", located ahead of and generally within 10-15 km of the low-level mesocyclone, and 4) the "far-field", located upstream (relative to near-surface winds) and generally >30 km from the low-level mesocyclone. In 2019, RAAVENs were operated in the near inflow, right flank, and left flank, with a single RAAVEN operated in each. In contrast, 2023 deployments involved RAAVENs in only the near inflow and left flank missions with two RAAVENs operated in stacked formation in the left flank.

https://doi.org/10.5194/essd-2026-134
Preprint. Discussion started: 20 April 2026

Sensor	Years Used	Quantities Measured	Sampling Rate	Accuracy (Manufacturer Specs)	Manufacturer Time Constant
Multi-hole Probe (**MHP**) thermo: E+E EE03	2019	Temperature Relative Humidity	1 Hz	±0.3K ±3%	Unknown
MHP differential pressure (for derived wind)	2019, 2023	Pressure	50 Hz	±1.5hPa	~0s
InterMet bead thermistor and IST HYT271 RH sensor (**iPTH**)	2023	Temperature Relative Humidity Pressure	10 Hz	±0.3K ±5% ±1.5hPa	< 5s < 4s ~0s
Vaisala RSS-421 (**RSS-421**)	2023	Temperature Relative Humidity Pressure	5 Hz	±0.2K ±3% ±1hPa	0.5s 0.3s ~0s
VectorNav VN-200 (**VectorNav**)	2019, 2023	Pressure Latitude Longitude Altitude Inertial velocity	100 Hz	± 1.5hPa 1 m 1 m 1.5 m <0.05 m/s	~0s

Table 1. Sensor specifications.

Across both the 2019 and 2023 field seasons, 88 RAAVEN flights were conducted totalling 57.5 hours (Table 2). Of these flights 79 (48.1 flight hours) were conducted during coordinated operations including 71 flights (44.2 flight hours) targeting supercells. Flight times were generally less than 90 minutes with most flights around 35 min (Figure 4).

4 Dataset overview

All files are available in NetCDF format in the Earth Observing Laboratory's (EOL) long-term field data archive (refer to the Data Availability section for more information). EOL is a part of the National Science Foundation's National Centre for Atmospheric Research. Two versions of RAAVEN data are available. "Corrected" files have been corrected for bias in RH and hysteresis in temperature and RH (described in more detail in Section 5.1). Data in "uncorrected" files do not include these corrections and also contain additional aircraft state variables for more advanced wind calibration and quality controlling.

All data variables (Table 3) are linearly interpolated to a uniform 10 Hz time series. Sampling rates for individual sensors are shown in (Table 1). Time is recorded as epoch time: seconds since 00:00 UTC 1 January 1970. A flag for aircraft flight state is included in the dataset ("Flight_State"). The flag uses a 3-digit code to indicate when it is on the ground, ascending, or turning:

- Hundreds place: 0, on the ground; 1, in flight
- Tens place: 0, Descending; 1, level; 2, ascending
- Ones place: 0, straight; 1, turning.

https://doi.org/10.5194/essd-2026-134
Preprint. Discussion started: 20 April 2026

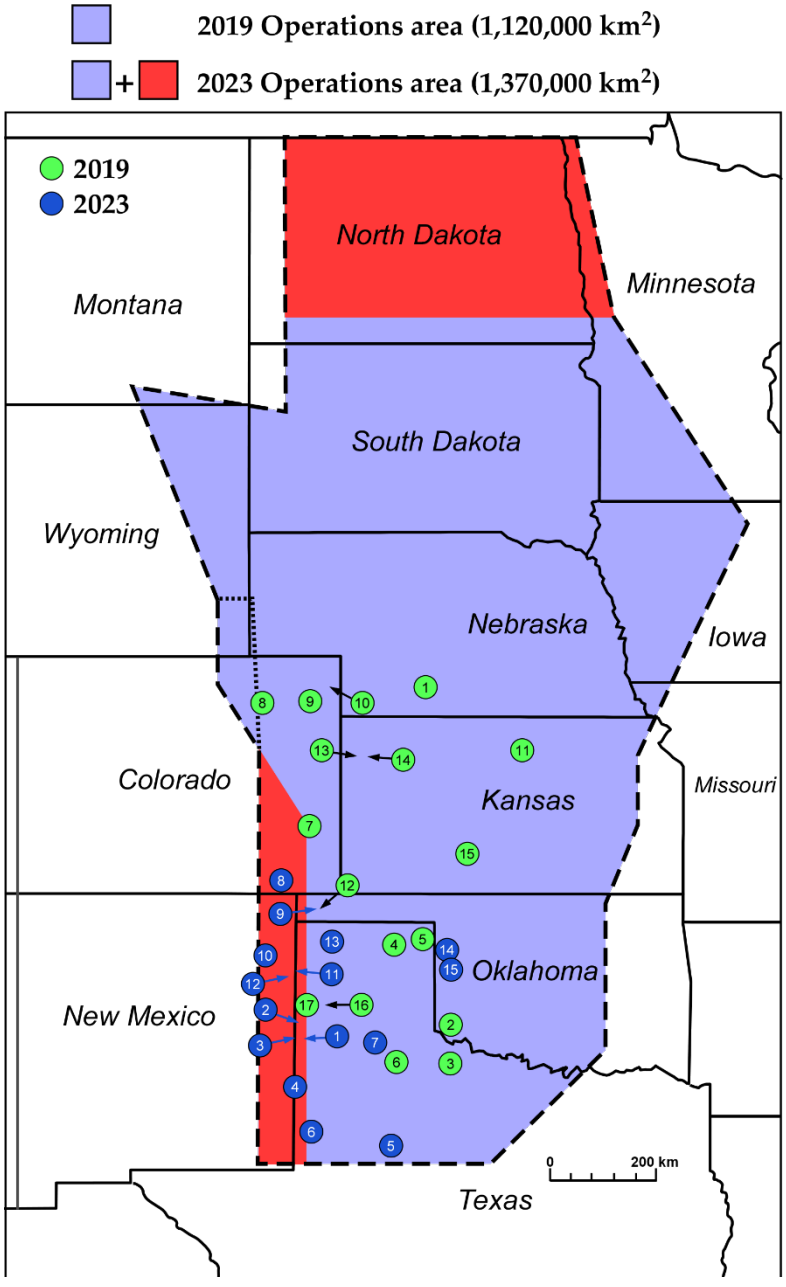

Figure 2: TORUS domains in 2019 and 2023 and individual deployment locations [adaptation of Fig. 4 from (Houston et al., 2026)]. Numbers indicate deployments, not necessarily separate storms.

https://doi.org/10.5194/essd-2026-134
Preprint. Discussion started: 20 April 2026

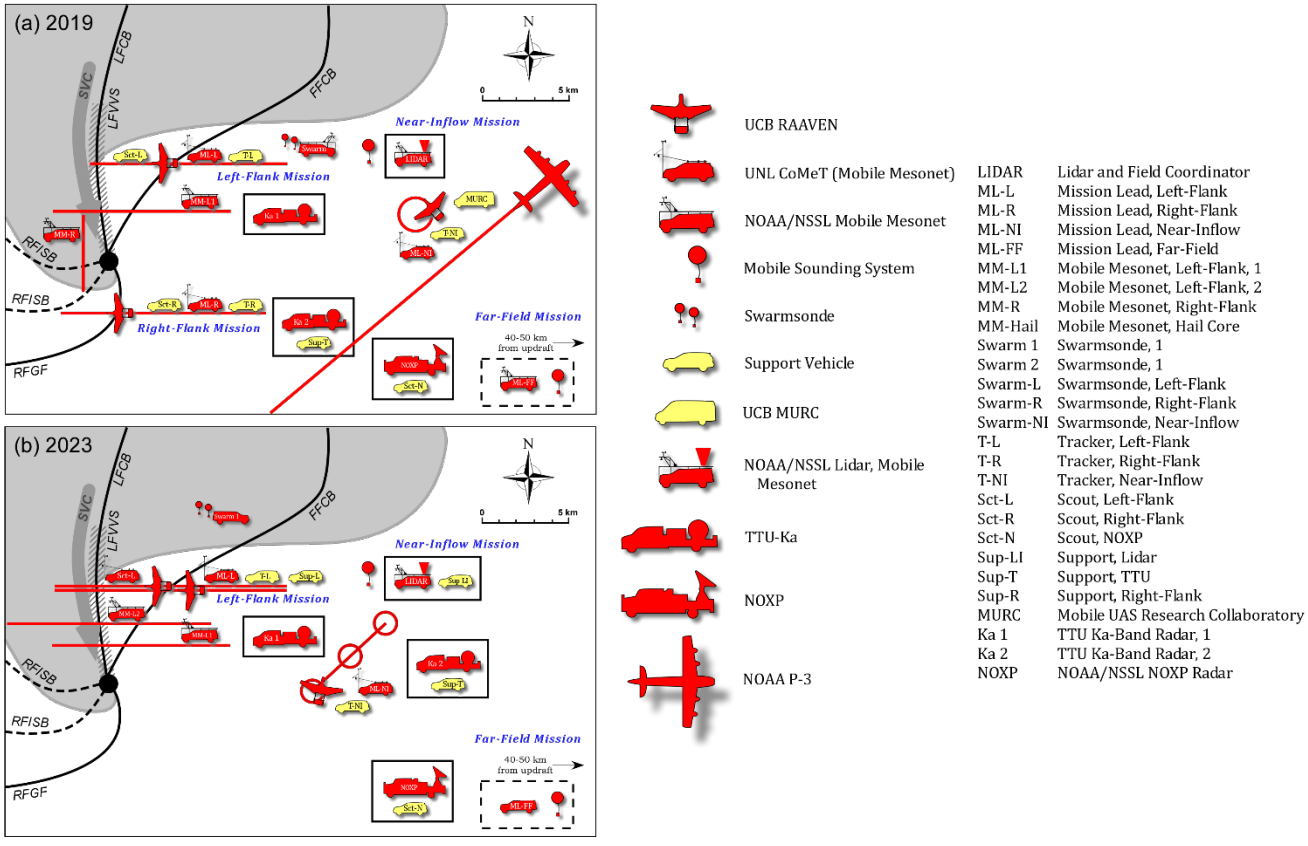

Figure 3: Adaptation of Fig. 2 from (Houston et al., 2026). Concepts of operations for each of the field seasons the RAAVEN was operated: a) 2019 and b) 2023. Shaded region indicates precipitation footprint, boundaries are indicated with black curves (LFCB – left-flank convergence boundary, FFCB – forward-flank convergence boundary, RFISB – rear-flank internal surge boundary, RFGF – rear-flank gust front), the centre of the near-surface circulation is annotated with a black circle, and the streamwise vorticity current (SVC) and left-flank vertical vorticity sheet (LFVVS) are illustrated with a grey arrow and hatching, respectively. Platforms coloured in red (yellow) are data collection (support) platforms. The "mission lead" designates the vehicle in which the person leading a particular mission resides. "Scout" vehicles are used as forward reconnaissance for hazard and/or platform siting identification. Platforms serve multiple functions. Platform name (e.g., "ML-L" – Mission Lead, left-flank) denotes their primary function. The icon also reflects their function and follows the symbol key (e.g., "Swarm1" has a primary function as a swarmsonde but is also a mobile mesonet). Red lines and circles indicate the storm-relative track of platforms during focused data collection (some ingress and egress routes are excluded). Black boxes indicate platforms that are fixed during focused data collection. Mission areas are labelled in blue.

Date	Location	Filename	Storm	Supercell	Mission	Flight time (min)	Shield. Temp. Rec.	Shield. RH Rec.	Exp. Temp. Rec.	Exp. RH Rec.	Wind Rec.
2019-05-15	[Testing]	RAAVEN_2_20190515_213742			N/A	10.1	0%	0%	100%	100%	98%
	[Testing]	RAAVEN_5_20190515_212057			N/A	53.6	0%	0%	100%	100%	45%
2019-05-16	[Testing]	RAAVEN_2_20190516_221859			N/A	78.5	0%	0%	100%	100%	100%
	[Testing]	RAAVEN_5_20190516_213511			N/A	36.5	0%	0%	100%	100%	99%
2019-05-17	Farnam, NE	RAAVEN_2_20190517_232250	X	X	R	64.8	0%	0%	100%	100%	100%
	Farnam, NE	RAAVEN_4_20190517_231633	X	X	N	3.1	0%	0%	100%	100%	94%
	Farnam, NE	RAAVEN_4_20190517_232938	X	X	N	8.3	0%	0%	100%	100%	98%
	Farnam, NE	RAAVEN_4_20190518_001848	X		N	7.0	0%	0%	100%	100%	97%
	Farnam, NE	RAAVEN_5_20190517_231416	X	X	L1	70.2	0%	0%	100%	100%	96%
2019-05-18	Cherokee, OK	RAAVEN_5_20190518_231340	X		N/A	35.2	0%	0%	100%	100%	96%
2019-05-20	Mangum, OK	RAAVEN_2_20190520_212753	X	X	R	40.0	0%	0%	100%	100%	98%
	Vernon, TX	RAAVEN_2_20190521_005124	X	X	L1	16.2	0%	0%	100%	100%	99%
	Mangum, OK	RAAVEN_4_20190520_210720	X	X	N	52.3	0%	0%	100%	100%	100%
	Mangum, OK	RAAVEN_5_20190520_205152	X	X	L1	26.1	0%	0%	100%	100%	56%
	Vernon, TX	RAAVEN_5_20190521_004810	X	X	L2	22.0	0%	0%	100%	100%	81%
2019-05-23	Pampa, TX	RAAVEN_2_20190523_235849	X	X	R	65.9	0%	0%	0%	0%	100%
	Pampa, TX	RAAVEN_5_20190523_235740	X	X	L1	22.7	0%	0%	100%	100%	91%
2019-05-24	Matador, TX	RAAVEN_5_20190524_200735	X	X	L1	23.9	0%	0%	100%	100%	62%
2019-05-26	Lamar, CO	RAAVEN_5_20190526_212944	X	X	L1	43.1	0%	0%	100%	100%	98%
2019-05-27	Fort Morgan, CO	RAAVEN_2_20190527_202153	X	X	L1	21.2	0%	0%	100%	100%	99%
	Yuma, CO	RAAVEN_2_20190527_225651	X	X	L1	29.7	0%	0%	71%	71%	82%
2019-05-28	Tipton, KS	RAAVEN_3_20190528_224033	X	X	L1	46.5	0%	0%	100%	100%	89%
	Tipton, KS	RAAVEN_4_20190528_225339	X	X	N	34.8	0%	0%	100%	100%	99%
2019-06-02	Boise City, OK	RAAVEN_3_20190603_002929	X	X	L1	32.8	0%	0%	100%	100%	99%
	Boise City, OK	RAAVEN_4_20190603_003551	X	X	N	15.0	0%	0%	100%	100%	99%
2019-06-08	Goodland, KS	RAAVEN_3_20190608_210942	X	X	L1	46.9	0%	0%	100%	100%	90%
	Goodland, KS	RAAVEN_4_20190609_003216	X	X	N	39.9	0%	0%	100%	100%	99%
	Goodland, KS	RAAVEN_5_20190608_212442	X	X	R	38.5	0%	0%	100%	100%	99%

https://doi.org/10.5194/essd-2026-134
Preprint. Discussion started: 20 April 2026

Open Access Earth System Science Data Discussions

2019-06-11	Liberal, KS	RAAVEN_3_20190611_204702			N/A	60.8	0%	0%	100%	100%	96%
	Greensburg, KS	RAAVEN_3_20190612_000739	X	X	L1	84.0	0%	0%	100%	100%	100%
	Liberal, KS	RAAVEN_4_20190611_205454			N	37.0	0%	0%	100%	100%	87%
	Liberal, KS	RAAVEN_5_20190611_204514			N/A	30.2	0%	0%	100%	100%	99%
	Greensburg, KS	RAAVEN_5_20190612_010018	X	X	R	33.3	0%	0%	100%	100%	20%
2019-06-13	Boise City, OK	RAAVEN_2_20190614_004231	X		N/A	47.0	0%	0%	100%	100%	98%
	Boise City, OK	RAAVEN_4_20190613_190824	X		N	0.2	0%	0%	100%	100%	7%
	Boise City, OK	RAAVEN_5_20190614_003606	X		N/A	15.6	0%	0%	100%	100%	99%
2019-06-14	[Testing]	RAAVEN_0_20190614_205854			N/A	86.6	0%	0%	100%	100%	99%
	[Testing]	RAAVEN_2_20190614_211605			N/A	93.1	0%	0%	100%	100%	100%
	[Testing]	RAAVEN_4_20190614_210427			N/A	83.1	0%	0%	100%	100%	100%
2019-06-15	Vega, TX	RAAVEN_0_20190615_222434	X	X	R	58.9	0%	0%	100%	100%	99%
	Vega, TX	RAAVEN_0_20190615_235524	X	X	R	37.6	0%	0%	100%	100%	80%
	Vega, TX	RAAVEN_2_20190615_222915	X	X	L1	79.4	0%	0%	100%	100%	89%
	Vega, TX	RAAVEN_2_20190616_000159	X	X	L1	20.4	0%	0%	100%	100%	82%
	Vega, TX	RAAVEN_4_20190615_223449	X	X	N	7.1	0%	0%	100%	100%	96%
	Vega, TX	RAAVEN_4_20190615_231508	X	X	N	20.7	0%	0%	34%	34%	99%
	Vega, TX	RAAVEN_4_20190616_001324	X	X	N	8.2	0%	0%	100%	100%	80%
2023-05-23	Clovis, NM	RAAVEN_5_20230523_224728	X	X	N	17.0	0%	0%	100%	100%	95%
	Clovis, NM	RAAVEN_8_20230523_223440	X	X	L1	12.1	100%	0%	100%	100%	92%
	Clovis, NM	RAAVEN_9_20230523_223232	X	X	L2	50.8	81%	81%	100%	100%	62%
2023-05-24	Grady, NM	RAAVEN_9_20230524_233632	X	X	L2	35.7	100%	100%	100%	100%	95%
	Grady, NM	RAAVEN_8_20230525_002536	X	X	L1	35.1	82%	0%	100%	100%	87%
2023-05-25	[Testing]	RAAVEN_5_20230525_202640			N/A	92.6	0%	0%	100%	100%	99%
2023-05-26	Clovis, NM	RAAVEN_5_20230527_003616	X	X	N	63.6	0%	0%	100%	100%	98%
	Clovis, NM	RAAVEN_8_20230527_002328	X	X	L1	81.4	98%	98%	100%	100%	47%
	Clovis, NM	RAAVEN_9_20230527_002536	X	X	L2	85.2	100%	100%	100%	100%	99%
2023-05-27	Plains, TX	RAAVEN_5_20230527_234048	X	X	N	44.2	0%	0%	100%	100%	17%
	Plains, TX	RAAVEN_5_20230528_010608	X	X	N	16.9	0%	0%	100%	100%	0%
	Plains, TX	RAAVEN_8_20230527_233632	X	X	L1	71.1	100%	100%	100%	100%	92%

https://doi.org/10.5194/essd-2026-134
Preprint. Discussion started: 20 April 2026

Open Access Earth System Science Data Discussions

	Plains, TX	RAAVEN_9_20230527_230016	X	X	L2	75.3	100%	100%	100%	100%	73%
2023-05-31	[Testing]	RAAVEN_5_20230531_222816			N/A	30.2	0%	0%	100%	100%	13%
2023-06-01	Colorado City, TX	RAAVEN_5_20230601_230432	X	X	N	11.8	0%	0%	100%	100%	0%
	Colorado City, TX	RAAVEN_8_20230601_225808	X	X	L1	31.5	100%	100%	100%	100%	97%
	Colorado City, TX	RAAVEN_9_20230601_225808	X	X	L2	36.4	100%	100%	100%	100%	97%
2023-06-02	Hobbs, NM	RAAVEN_5_20230602_182712	X	X	N	47.6	0%	0%	100%	100%	98%
	Hobbs, NM	RAAVEN_8_20230602_182920	X	X	L1	35.6	75%	75%	100%	100%	81%
	Hobbs, NM	RAAVEN_9_20230602_182920	X	X	L2	44.4	100%	100%	100%	100%	83%
2023-06-09	Silverton, TX	RAAVEN_2_20230609_222816	X	X	N	32.4	0%	0%	100%	100%	81%
	Silverton, TX	RAAVEN_7_20230609_221320	X	X	L1	38.7	100%	100%	100%	100%	98%
	Silverton, TX	RAAVEN_9_20230609_221528	X	X	L2	43.3	100%	100%	100%	100%	98%
2023-06-11	Kim, CO	RAAVEN_2_20230611_215408	X	X	N	43.9	0%	0%	100%	100%	98%
	Boise City, OK	RAAVEN_2_20230612_010152	X	X	N	23.7	0%	0%	100%	100%	96%
	Kim, CO	RAAVEN_7_20230611_215616	X	X	L1	34.5	98%	98%	100%	100%	96%
	Boise City, OK	RAAVEN_7_20230612_005944	X	X	L1	41.2	100%	100%	100%	100%	95%
	Kim, CO	RAAVEN_9_20230611_221112	X	X	L2	39.1	100%	100%	100%	100%	81%
	Boise City, OK	RAAVEN_10_20230612_005944	X	X	L2	40.9	100%	100%	100%	100%	96%
2023-06-12	Nara Visa, NM	RAAVEN_2_20230612_231928	X	X	N	46.6	0%	0%	100%	100%	98%
	Bueyeros, NM	RAAVEN_5_20230612_205216	X	X	N	50.2	0%	0%	100%	100%	97%
	Bueyeros, NM	RAAVEN_6_20230612_210256	X	X	L1	64.0	100%	100%	100%	100%	99%
	Nara Visa, NM	RAAVEN_6_20230612_231512	X	X	L1	17.0	100%	100%	100%	100%	66%
	Nara Visa, NM	RAAVEN_9_20230613_000832	X	X	L1	6.2	100%	100%	100%	100%	92%
	Bueyeros, NM	RAAVEN_10_20230612_210256	X	X	L2	67.8	100%	100%	100%	100%	95%
	Nara Visa, NM	RAAVEN_10_20230612_231720	X	X	L2	18.0	100%	100%	100%	100%	82%
2023-06-13	Conlen, TX	RAAVEN_2_20230613_221528	X	X	N	15.6	0%	0%	100%	100%	95%
	Conlen, TX	RAAVEN_6_20230613_215241	X	X	L1	37.3	100%	100%	0%	0%	85%
2023-06-15	Arnett, OK	RAAVEN_2_20230616_000001	X	X	N	12.1	0%	0%	100%	100%	94%
	Arnett, OK	RAAVEN_6_20230615_235544	X	X	L1	29.4	100%	100%	100%	100%	95%
	Arnett, OK	RAAVEN_9_20230615_231056	X	X	L1	6.6	100%	100%	100%	100%	89%
	Arnett, OK	RAAVEN_9_20230615_235752	X	X	L2	33.4	100%	100%	100%	100%	82%

Table 2. Summary of all RAAVEN flights. Date in the first column is based on local time. The filename is listed as RAAVEN_[#]_[YYYMMDD]_[hhmmss] where # is the RAAVEN number and YYYYMMDD and hhmmss are the year, month, day and hour, minute, and seconds, respectively, in GMT, corresponding to VectorNav GPS lock time, not necessarily takeoff time. Storm (supercell) columns indicate whether there was a target storm (supercell) present. Mission key is as follows: N, near-inflow; LF1, lower altitude left-flank; LF2, upper altitude left-flank; RF, right-flank. The last 5 columns are the percentage of the data file that has "good" records (see text) for shielded temperature, shielded RH, exposed temperature, exposed RH, and wind, respectively.

Short Name	Long Name	Description	Units	Presence in Datasets	Sensors Used
time	time	Timestamp at 10 Hz	UTC timestamp	2019, 2023	VectorNav
lat	Latitude	Aircraft latitude	Degrees north	2019, 2023	VectorNav
lon	Longitude	Aircraft longitude	Degrees east	2019, 2023	VectorNav
alt	Altitude	Drift-corrected aircraft altitude above mean sea level.	meters	2019, 2023	VectorNav
flight_state	Flight State	Flag to indicate aircraft flight state	N/A	2019, 2023	VectorNav
air_temp_exp	Exposed Air Temperature	Air Temperature from unshielded sensor	Kelvin	2019, 2023	MHP (2019) RSS-421 (2023)
air_rh_exp	Exposed Air Relative Humidity	Relative Humidity from unshielded sensor	%	2019, 2023	MHP (2019) RSS-421 (2023)
flag_exp	Exposed Sensor Quality Flag	Flag for possible sensor wetting	N/A	2019, 2023	
air_temp_shield	Shielded Air Temperature	Hysteresis corrected air temperature from shielded sensor	Kelvin	2023	iPTH
air_rh_shield	Shielded Relative Humidity	Bias corrected air relative humidity from shielded sensor	%	2023	iPTH
flag_shield	Shielded Temperature Sensor Flag	Flag for specific iPTH sensor used	N/A	2023	
pressure	Static Pressure	Static Pressure	hPa	2019, 2023	VectorNav
u	Eastward Wind	Zonal wind speed	m/s	2019, 2023	MHP, VectorNav, exposed temp. sensor
v	Northward Wind	Meridional wind speed	m/s	2019, 2023	MHP, VectorNav, exposed temp. sensor
w	Vertical Wind	Vertical wind speed	m/s	2019, 2023	MHP, VectorNav, exposed temp. sensor
u_uncertainty	Eastward Wind Uncertainty	Absolute zonal wind speed uncertainty	m/s	2019, 2023	MHP, VectorNav, exposed temp. sensor
v_uncertainty	Northward Wind Uncertainty	Absolute meridional wind speed uncertainty	m/s	2019, 2023	MHP, VectorNav, exposed temp. sensor
w_uncertainty	Vertical Wind Uncertainty	Absolute vertical wind speed uncertainty	m/s	2019, 2023	MHP, VectorNav, exposed temp. sensor
VE	eastward_platform_speed_wrt_ground	Aircraft Eastward Ground Velocity	m/s	2019, 2023	VectorNav
VN	northward_platform_speed_wrt_ground	Aircraft Northward Ground Velocity	m/s	2019, 2023	VectorNav
VD	downward_platform_speed_wrt_ground	Aircraft Downward Ground Velocity	m/s	2019, 2023	VectorNav
TAS	True airspeed	Airspeed of the aircraft	m/s	2019, 2023	MHP, VectorNav, exposed temp. sensor, autopilot

wind_flag	Wind sensor quality flag	Composite of individual sensor flags and checks wind magnitudes and uncertainties	N/A	2019, 2023	
roll	Aircraft Roll	Aircraft Roll	Degrees	2019, 2023	Autopilot
pitch	Aircraft Pitch	Aircraft Pitch	Degrees	2019, 2023	Autopilot
yaw	Aircraft Yaw	Aircraft Yaw	Degrees	2019, 2023	Autopilot

Table 3. Description of variables in data files. Variables in shaded rows are only in the uncorrected files. Refer to Table 1 for sensor names.

https://doi.org/10.5194/essd-2026-134
Preprint. Discussion started: 20 April 2026

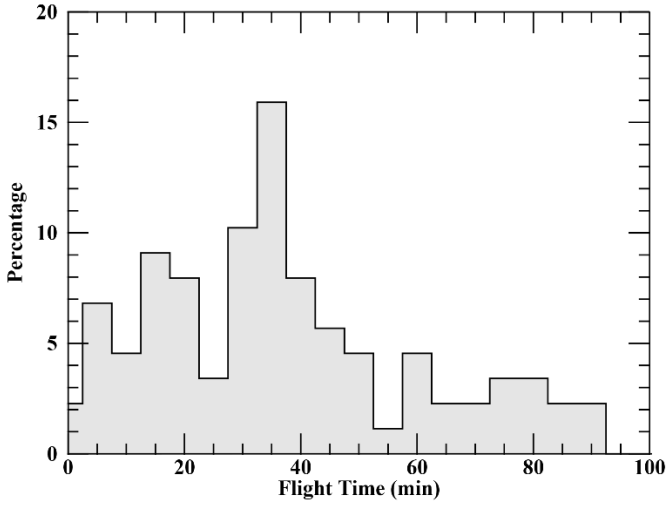

Figure 4: Distribution of flight times binned at 5 min increments.

5 Data Processing

5.1 Thermodynamic Data

As described by Axon et al. (2024), the MHP temperature/humidity sensor used in 2019 had an ~11-second 63.2% response time lag. A first-order hysteresis correction is applied to MHP temperature and humidity data using the equation,

$$Z_c = \tau \frac{dZ}{dt} + \hat{Z} \quad (1)$$

where Z_c is the corrected observation, $\frac{dZ}{dt}$ is the center difference of the raw observations, $\hat{Z}$ is the observation to be corrected, and τ is the 63.2% time constant. A gaussian-weighted rolling boxcar smoother of width τ is applied to the raw data prior to correction to reduce the magnification of random noise.

The MHP-based temperature and humidity data are recorded in the "exposed" variables (Table 3) because the upward-facing aspiration vent for the sensor is not shielded from precipitation or insolation. A quality flag is included to note data that might be contaminated by precipitation: a value of 0 denotes data likely not affected by wetting and a value of 1, denotes questionable data. Data are flagged as questionable when there are *both* indications of wetting in the MHP temperature and humidity data and indications of precipitation in radar data coincident with the aircraft. Typical indicators for wetting are sudden reductions in temperature and a slow (relative to the reduction) relaxation back to ambient conditions, coupled with increases in relative humidity (Figure 5a-c). While corrections accounting for wetting would be preferred to simple flagging, as noted by Eastin et al. (2002), "analytic corrections for a wet sensor are difficult without knowledge of the fractional surface area of the sensor that is wetted". Wetting of the MHP sensor was identified in 18.4% of all RAAVEN observations for storm deployments (Table 4). The fraction was much lower (0.7%) for near-inflow flights and much higher (30.7%) for

https://doi.org/10.5194/essd-2026-134
Preprint. Discussion started: 20 April 2026

Open Access Earth System Science Data Discussions

left-flank flights (Table 4). Instances in which either uncorrected temperature or uncorrected RH data are deemed physically unrealistic, are removed from the dataset and replaced with NaN.

In datasets from 2023, the RSS-421 sensors (Table 3) are reported as "exposed" quantities. Since two sensors are available, the value of temperature or relative humidity reported is selected through application of the following algorithm (hereafter referred to as the "sensor selection algorithm"):

1. The total number of erroneous data points (listed in the raw data as -999) for each sensor on a given flight is determined.
2. Data from the sensor with the fewest erroneous data points are reported in the data file.

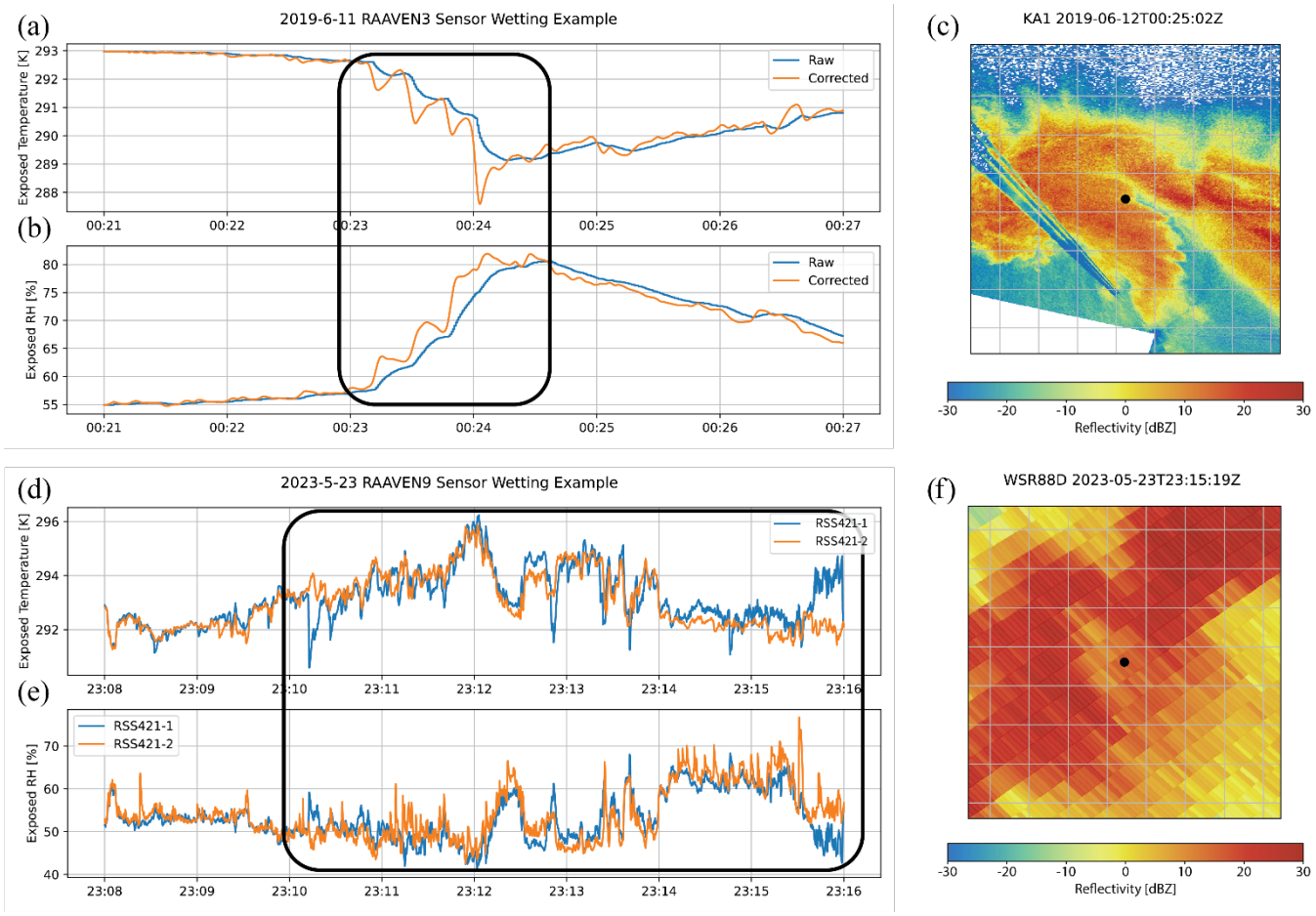

Figure 5: Examples of sensor wetting events in RAAVEN data (annotated with rounded rectangles) for the MHP sensor (a-c on 11 June 2019, local time) and RSS-421 (d-f on 23 May 2023). a) MHP temperature (K) for the hysteresis-corrected (orange) and uncorrected (blue) data; b) relative humidity (%) for the hysteresis-corrected (orange) and uncorrected (blue) data; c) radar reflectivity factor from the Texas Tech Ka-band radar at 00:25:02 GMT with the position of the RAAVEN indicated with a black dot; d) RSS-421 temperature (K) for the two RSS-421 sensors; e) relative humidity (%); f) WSR-88D radar reflectivity factor data at 23:15:19 GMT, corresponding to the wetting event later in the illustrated time series, with the position of the RAAVEN indicated with a black dot.

https://doi.org/10.5194/essd-2026-134
Preprint. Discussion started: 20 April 2026

Open Access Earth System Science Data Discussions

Mission	Wet MHP (2019 only)	Wet RSS421 (2023 only)	iPTH Temp. (2023 only)	High iPTH RH (2023 only)	Suspect Wind
All storms	18.4%	19.1%	26.6%	2.8%	4.8%
Near Inflow	0.7%	11.3%	N/A	N/A	7.3%
Left-Flank	30.7%	22.2%	26.6%	2.8%	5.0%
Right-Flank	10.9%	N/A	N/A	N/A	3.7%

Table 4. Fractional occurrence of flags used. The wet MHP statistics are for 2019 only and are the number of the times the flag was set relative to the number of times the MHP temperature was reporting physically reasonable values. The wet RSS-421 statistics are for 2023 only and are the number of the times the flag was set relative to the number of times the RSS-421 temperature was reporting physically reasonable values. The iPTH temperature statistics are for 2023 only and are the number of times that the dedicated iPTH temperature and not the backup iPTH temperature (RH temperature) was used relative to the number of times either the dedicated iPTH temperature or the backup iPTH temperature were reporting. The high iPTH RH statistics are for 2023 only and are the number of times the relative humidity exceeded 98% relative to the number of times that physically reasonable iPTH RH values were reported. The suspect wind statistics are the number of times that suspect winds were flagged (refer to Section 5.2) relative to the number of times at least one valid wind component was reported.

Any remaining erroneous data points in the reported data are replaced with data from the other RSS-421 sensor. Like the MHP in 2019, the RSS-421 sensors were exposed to precipitation and showed signs of sensor wetting. The same flagging procedure described above is applied to the RSS-421 data. An example of likely wetting of the RSS-421 sensor is illustrated in Figure 5d-f. Instances of RSS-421 wetting (Table 4) were slightly more common overall (19.1%) than MHP wetting (18.4%), largely driven by more frequent instances of wetting for the near-inflow flights (11.3% compared to 0.7%).

The dedicated iPTH temperature thermistor used in the shielded sensor set in 2023 experienced frequent dropouts, only functioning 26.6% of the time (Table 4). A backup temperature sensor within the relative humidity sensor (referred to as RH temperature) was present but had a comparatively slow response (Figure 6). When available, the dedicated iPTH temperature was reported as the shielded temperature; in the remaining cases, a hysteresis-corrected RH temperature was used instead. The "flag_shield" variable within the dataset is an indicator of which sensor is selected: 0 for when the dedicated iPTH temperature is used or 1 when the hysteresis-corrected RH temperature is used. The 63.2% time constant for each RAAVEN's RH temperature sensor was determined based on root mean square error (RMSE) analysis between the fast response RSS-421 and slower RH across all datasets for a given RAAVEN and a range of time constants (Figure 7). The single time constant used for the hysteresis correction (applied using (1)) of all iPTH RH temperature observations for each RAAVEN is listed in Table 5.

RMSE analysis also indicated a bias in the iPTH RH measurements. Based on humidity chamber experiments conducted by A. Segales at the University of Oklahoma using the same type of sensors, it was concluded that the humidity bias scales with true humidity and temperature following a 4th order (humidity) and first order (temperature) correction equation:

$$R = 13.68 + 0.1244\,R_0 + 0.0334\,R_0^2 - 3.154\cdot10^{-4}\,R_0^3 + 4.864\cdot10^{-7}\,R_0^4 \\ -0.03791\,T + 1.814\cdot10^{-3}\,R_0\,T - 6.892\cdot10^{-5}\,R_0^2\,T + 5.87\cdot10^{-7}\,R_0^3\,T$$

where R is corrected relative humidity, R_0 is uncorrected relative humidity, and T is fast temperature (or hysteresis-corrected RH temperature). By coupling the corrected RH to fast temperature, this approach also obviates the need for separate

https://doi.org/10.5194/essd-2026-134
Preprint. Discussion started: 20 April 2026

Open Access Earth System Science Data Discussions

hysteresis correction of RH. Biases in RH for a specific sensor might still exist even after this correction, but comparisons with RSS-421 observations yield general consensus between sensors across all cases when the correction is applied. Due to limitations of the experiments conducted by A. Segales, the correction can create RH values >100% when applied to uncorrected RH >94%. Thus, the reported RH is clipped to not exceed 99.9%. Reported RH values >98% only occur 2.8% of the time (Table 4).

Multiple pressure sensors were available for the final pressure reported in 2019 and 2023: VectorNav and MHP in 2019 and VectorNav, MHP, RSS-421s, and iPTH in 2023. Analysis shows no sensor necessarily represents the ambient pressure better than any other, and overall reliability of the sensor takes greater priority in sensor selection. The VectorNav proved to be the most reliable sensor and is therefore used exclusively.

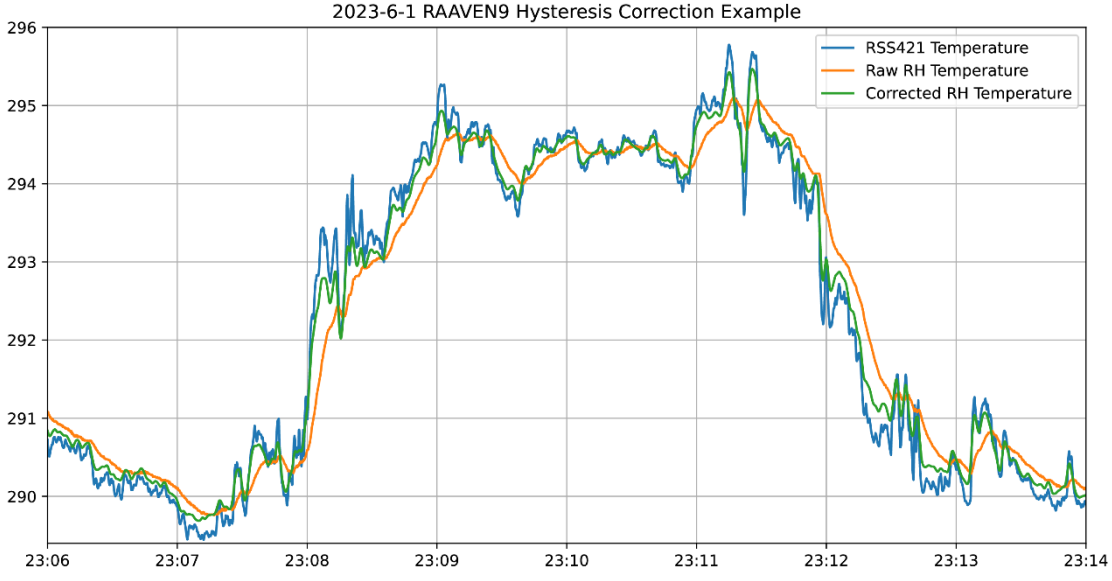

Figure 6. Example comparison of the slow-responding RH temperature (orange curve) in the iPTH sensor set to the fast-responding RSS-421 (blue curve). The corrected RH temperature is also illustrated (green curve).

RAAVEN Number	iPTH RH Temperature Time Constant
6	19 seconds
7	4 seconds
8	15 seconds
9	6 seconds
10	12 seconds

Table 5. Time constants used for hysteresis corrections applied to the backup RH temperature sensor in 2023.

https://doi.org/10.5194/essd-2026-134
Preprint. Discussion started: 20 April 2026

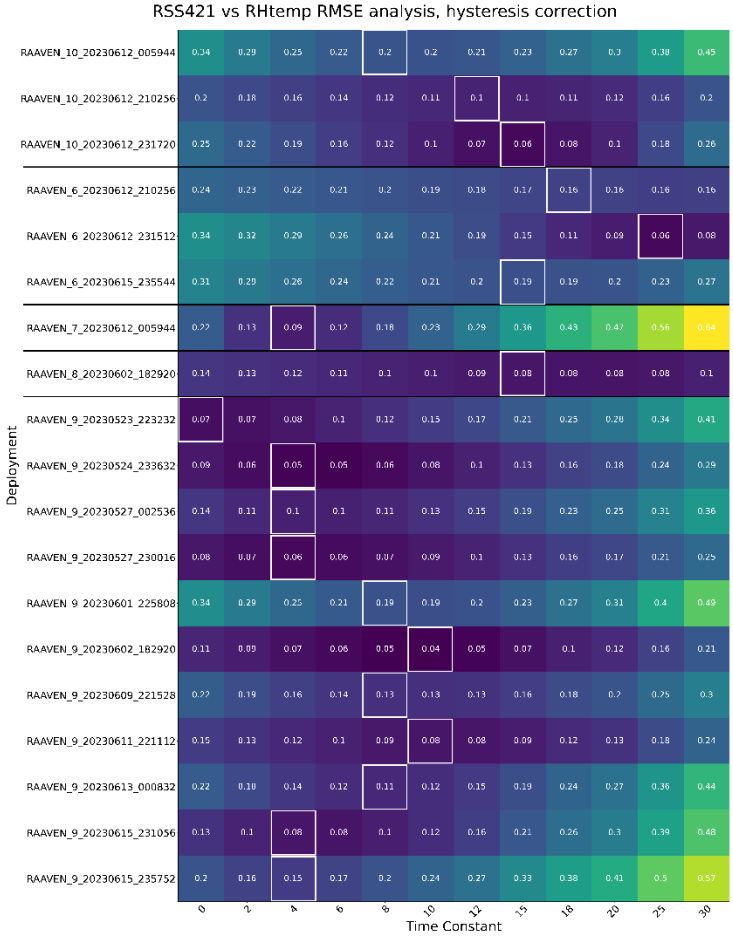

Figure 7. RMSE values plotted as a function of 63.2% time constant for the (backup) iPTH RH temperature using RSS-421 RH as reference. Each data set for each RAAVEN is considered where RAAVEN number, date, and time follow the conventions used in Table 2. White boxes indicate the minimum RMSE and black lines separate RAAVEN numbers.

5.2 Wind Data

Inertial wind components are derived from both multi-hole probe and inertial navigation system measurements. The differential pressure measurements from each multi-hole probe port (Figure 8) are first used to estimate air-relative velocity through a wind-tunnel-calibrated polynomial fit (Sasse and Argrow, 2022).

Air-relative velocity components are then combined with aircraft inertial velocity and attitude measurements from the VectorNav inertial navigation system to obtain inertial wind velocity through the Lenschow wind approximation (Lenschow and Spyers-Duran, 1989).

Directly computed wind estimates are refined through a bias correction process (De Boer et al., 2022a). This optimization searches a parameter space of up to ±10% airspeed bias, ±20 ms time lag in the inertial measurement system, and up to ±5°

https://doi.org/10.5194/essd-2026-134
Preprint. Discussion started: 20 April 2026

of offset in the probe air-relative velocity angles to minimize the yaw-correlated variance in streamwise wind perturbations. The noise standard deviation of the derived inertial wind product is computed from propagated instrument uncertainties for each wind component (Sasse et al., 2024; Sasse, 2025). Corrected inertial winds are saved as zonal (u), meridional (v), and vertical (w) components. Associated uncertainties are represented by a single standard deviation. Both winds and uncertainties are reported in m/s.

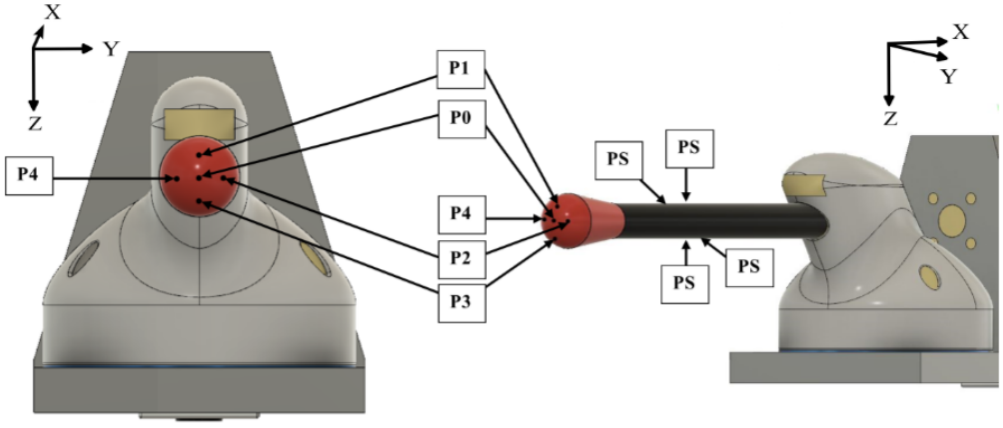

Figure 8. Multi-hole probe port layout.

A flag for unreliable wind measurements (the "wind_flag" variable) is also included as the composite of individual sensor flags, as well as checks on reasonable wind magnitudes and uncertainties. This includes the following data points:

- Differential pressure measurements outside of sensor capability thresholds
- Wind angles greater than 45 degrees
- Inertial wind components greater than 50 m/s
- Inertial wind component uncertainties greater than 30 m/s
- Regions where the moving standard deviation of the signal over 20 seconds exceeds 7 m/s and the periodicity of the signal – as the normalized autocorrelation function maximum at lag indices greater than 10 – exceeds 0.3.

Wind variables where the differential pressures, wind angles, or absolute wind components fail the quality control check are set to NaN, while wind values for moving-variance or uncertainty failures are retained but flagged. Suspect winds were flagged 4.8% of the time across all flights and were most common in near inflow flights (Table 4).

Uncertainty PDFs (Figure 9a-c) are very similar across the three mission areas with generally larger uncertainties for u and v components than the w component of the wind. CDFs (Figure 9d-f) indicate more than 85% of uncertainty values for u and v components are less than 2 m/s while more than 95% of uncertainty values for w are less than 1 m/s. Vertical velocity distributions for the three mission areas (Figure 10) show that vertical motion in near-inflow flights are generally smaller in magnitude than in left- and right-flank missions. This signal is to be expected considering that, unlike the other missions,

https://doi.org/10.5194/essd-2026-134
Preprint. Discussion started: 20 April 2026

near-inflow flights are conducted upstream of the storm away from the deep convective updraft and forced ascent along airmass boundaries. The vertical motion observed by the near inflow mission also exhibits a slight bias towards downward motion, consistent with its placement in gentle subsidence away from the storm.

Vertical velocity distributions as a function of height are wider through the entire flight depths for the left/right-flank flights compared to near inflow flights (Figure 11a-c). Median wind speeds are generally similar across the collection of near inflow and left-flank flights (Figure 11d-e) though higher in right-flank flights (Figure 11f). Wind speeds in the 75^{th}-90^{th} percentiles are higher in the left/right-flanks than the near inflow; an unsurprising result considering the focus of these flights within storm generated outflow.

https://doi.org/10.5194/essd-2026-134
Preprint. Discussion started: 20 April 2026

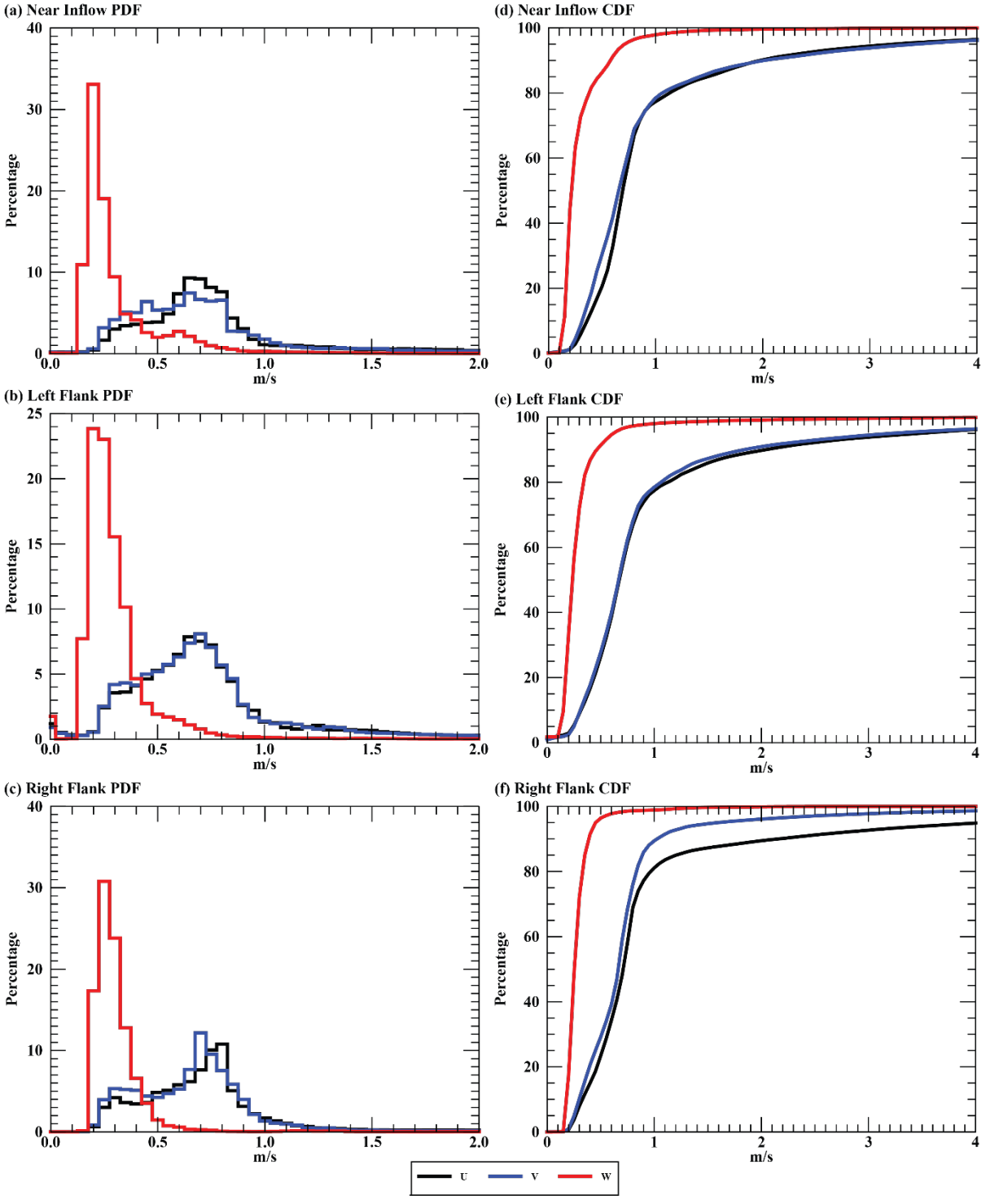

Figure 9. PDFs (a-c) and CDFs (d-f) of the absolute value of uncertainties for u (black), v (blue), and w (red) components of the wind separated into flight missions in the near inflow (a, d), left-flank (b, e), and right-flank (c, f).

https://doi.org/10.5194/essd-2026-134
Preprint. Discussion started: 20 April 2026

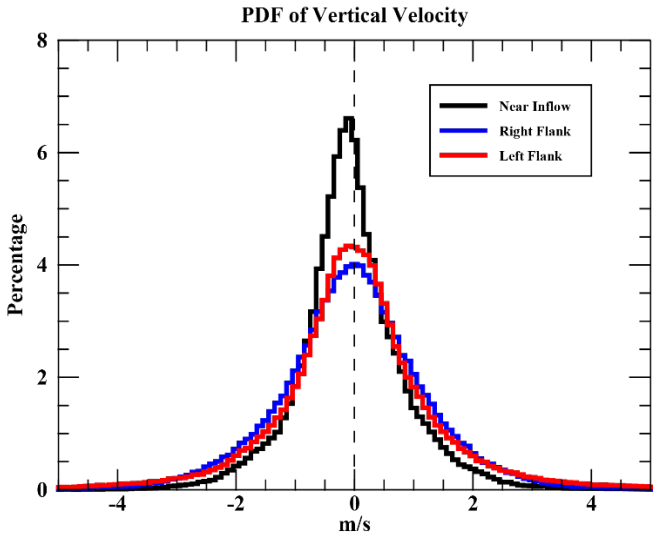

Figure 10. PDFs for the w component of the wind for flights in the near inflow (black), right flank (blue), and left flank (red) missions. Only vertical motions with uncertainties < 1 m/s are included.

6. Summary

The quality control procedures adopted for RAAVEN UAS data collected during the 2019 field season of TORUS and TORUS-LItE (in 2023) were described. Despite extensive predeployment testing, the demanding environments where data collection occurred presented numerous challenges to data quality. Many of these procedures aim to quantify data-quality uncertainty, in lieu of correcting questionable data. Procedures address the dependency of estimated wind on aircraft manoeuvring, periodically faulty sensors, questionable data induced by sensor wetting in rain, and sensor hysteresis and bias. Statistics calculated across the entire datasets, typically compartmentalized into the three mission areas (near inflow, left-flank, and right-flank). Wind uncertainties were generally less than 2 m/s for horizontal wind components and less than 1 m/s for vertical motion. In-storm mission areas (i.e., flights in the storm left-flank and right-flank) had stronger vertical motion at all heights than the near-inflow flights ahead of the storm where a tendency for weak descending motion is seen.

https://doi.org/10.5194/essd-2026-134
Preprint. Discussion started: 20 April 2026

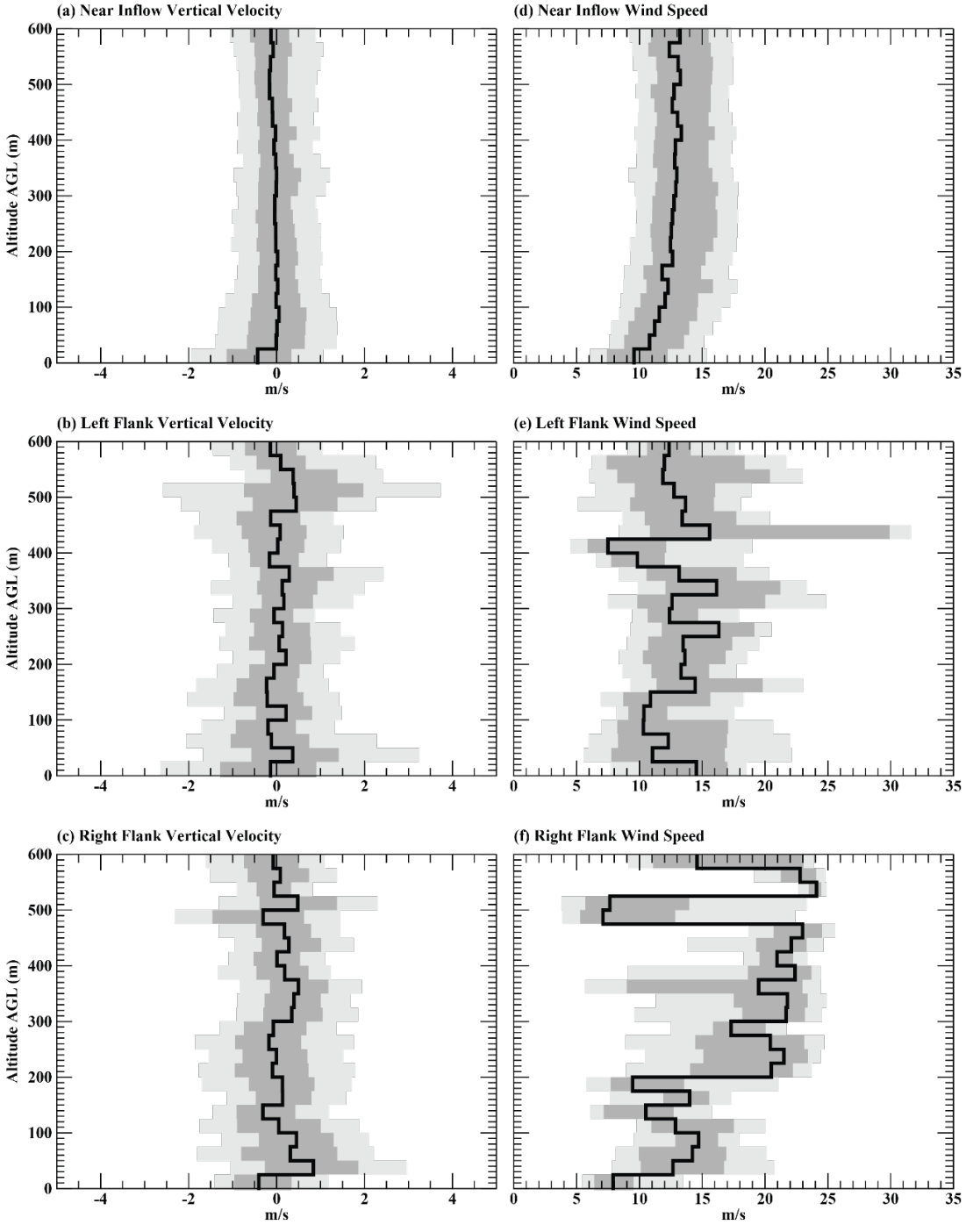

Figure 11. Vertical profiles of vertical velocity (a-c) and wind speed (d-f) for flights in the near inflow, left-flank, and right-flank mission areas. Flight data are binned in 25 m increments with the light (dark) grey area illustrating the 10th to 90th (25th to 75th) percentile and the black contour showing the median. Only wind speeds for uncertainties < 2 m/s and vertical velocities for uncertainties <1 m/s are included.

https://doi.org/10.5194/essd-2026-134
Preprint. Discussion started: 20 April 2026

Data and code availability

All TORUS RAAVEN data are available in the long-term field data archive of NCAR/EOL: https://doi.org/10.26023/FJD8-VMV2-XW0Y, https://doi.org/10.26023/E5PJ-5CN7-VQ0T (Argrow et al., 2026a, b). Python functions for smoothing, hysteresis correction, and iPTH RH correction are available on GitHub: https://github.com/markdebrstorms/UAS_Processing (De Bruin, 2026).

Author contributions

A. Houston calculated bulk statistics for the dataset and prepared the manuscript with contributions from all co-authors. He was also the thesis supervisor for M. De Bruin. M. De Bruin manually analysed all cases and developed and applied quality control code for thermodynamic quantities. C. Gomez-Faulk ran wind processing code and synthesized the final data sets. B. Argrow supervised C. Gomez-Faulk and supervised development of wind processing code.

Disclaimer

Copernicus Publications remains neutral with regard to jurisdictional claims made in the text, published maps, institutional affiliations, or any other geographical representation in this paper. While Copernicus Publications makes every effort to include appropriate place names, the final responsibility lies with the authors. Views expressed in the text are those of the authors and do not necessarily reflect the views of the publisher."

Acknowledgements

The authors wish to thank Dr. Robert Sasse for wind processing theory and code development and Dr. Tony Segales for running experiments to calibrate InterMet sensors. Thanks also go to Dr. Gijs de Boer for development of the algorithm to select RSS-421 sensor data to report in final data sets. The authors are grateful for the contributions from the University of Colorado Boulder and University of Nebraska-Lincoln students, staff, and affiliates without whom RAAVEN data collection during TORUS and TORUS-LItE would not have been possible.

Financial support

This work was supported by the National Science Foundation under grants AGS-1824609, AGS-1824649, AGS-2312996, and AGS-2312994.

https://doi.org/10.5194/essd-2026-134
Preprint. Discussion started: 20 April 2026

Review statement

The review statement will be added by Copernicus Publications listing the handling editor as well as all contributing referees according to their status anonymous or identified.

References

Argrow, B., Frew, E., Houston, A., De Bruin, M., and Gomez-Faulk, C.: TORUS 2019: RAAVEN UAS Data (1.1), Earth Observing Laboratory [dataset], https://doi.org/10.26023/FJD8-VMV2-XW0Y, 2026a.

Argrow, B., Frew, E., Houston, A., De Bruin, M., and Gomez-Faulk, C.: TORUS-LItE: RAAVEN UAS data (1.0), Earth Observing Laboratory [dataset], https://doi.org/10.26023/E5PJ-5CN7-VQ0T, 2026b.

Axon, K. L., Houston, A. L., Ziegler, C. L., Weiss, C. C., Rasmussen, E. N., Coniglio, M. C., Argrow, B., Frew, E., Swenson, S., Reinhart, A. E., and Wilson, M. B.: The Potential Roles of Preexisting Airmass Boundaries on a Tornadic Supercell Observed by TORUS on 28 May 2019, Mon. Wea. Rev., 152, 97-121, https://doi.org/10.1175/MWR-D-23-0007.1, 2024.

Cleary, P. A., de Boer, G., Hupy, J. P., Borenstein, S., Hamilton, J., Kies, B., Lawrence, D., Pierce, R. B., Tirado, J., Voon, A., and Wagner, T.: Observations of the lower atmosphere from the 2021 WiscoDISCO campaign, Earth Syst. Sci. Data, 14, 2129-2145, 10.5194/essd-14-2129-2022, 2022.

de Boer, G., Borenstein, S., Calmer, R., Cox, C., Rhodes, M., Choate, C., Hamilton, J., Osborn, J., Lawrence, D., and Argrow, B.: Measurements from the university of colorado raaven uncrewed aircraft system during atomic, Earth System Science Data, 14, 19-31, 2022a.

de Boer, G., Borenstein, S., Calmer, R., Cox, C., Rhodes, M., Choate, C., Hamilton, J., Osborn, J., Lawrence, D., Argrow, B., and Intrieri, J.: Measurements from the University of Colorado RAAVEN Uncrewed Aircraft System during ATOMIC, Earth Syst. Sci. Data, 14, 19-31, 10.5194/essd-14-19-2022, 2022b.

De Bruin, M.: UAS Processing, GitHub [code], https://github.com/markdebrstorms/UAS_Processing, 2026.

Eastin, M. D., Black, P. G., and Gray, W. M.: Flight-Level Thermodynamic Instrument Wetting Errors in Hurricanes. Part I: Observations, Mon. Wea. Rev., 130, 825-841, https://doi.org/10.1175/1520-0493(2002)130<0825:FLTIWE>2.0.CO;2, 2002.

Elston, J. S., Roadman, J., Stachura, M., Argrow, B., Houston, A. L., and Frew, E. W.: The Tempest unmanned aircraft system for in situ observations of tornadic supercells:Design and VORTEX2 flight results, Journal of Field Robotics, 28, 461-483, 10.1002/rob.20394, 2011.

Frew, E. W., Elston, J., Argrow, B., Houston, A. L., and Rasmussen, E. N.: Unmanned Aircraft Systems for Sampling Severe Local Storms and Related Phenomena, IEEE Robotics and Automation Magazine, 19, 85-95, 2012.

Holland, G. J., Webster, P. J., Curry, J. A., Tyrell, G., Gauntlett, D., Brett, G., Becker, J., Hoag, R., and Vaglienti, W.: The Aerosonde robotic aircraft: A new paradigm for environmental observations, Bulletin of the American Meteorlogical Society, 82, 889-901, 2001.

Houston, A. L., Argrow, B., Elston, J., Lahowetz, J., Frew, E. W., and Kennedy, P. C.: The Collaborative Colorado-Nebraska Unmanned Aircraft System Experiment, Bulletin of the American Meteorlogical Society, 93, 39-54, 10.1175/2011BAMS3073.1, 2012.

Houston, A. L., Weiss, C. C., Rasmussen, E. N., Coniglio, M. C., Ziegler, C. L., Argrow, B. M., and Frew, E. W.: Targeted Observation by Radars and UAS of Supercells: TORUS, Bulletin of the American Meteorological Society, BAMS-D-23-0265.0261, https://doi.org/10.1175/BAMS-D-23-0265.1, 2026.

Lappin, F., de Boer, G., Klein, P., Hamilton, J., Spencer, M., Calmer, R., Segales, A. R., Rhodes, M., Bell, T. M., Buchli, J., Britt, K., Asher, E., Medina, I., Butterworth, B., Otterstatter, L., Ritsch, M., Puxley, B., Miller, A., Jordan, A., Gomez-Faulk, C., Smith, E., Borenstein, S., Thornberry, T., Argrow, B., and Pillar-Little, E.: Data collected using small uncrewed aircraft systems during the TRacking Aerosol Convection interactions ExpeRiment (TRACER), Earth Syst. Sci. Data, 16, 2525-2541, 10.5194/essd-16-2525-2024, 2024.

Lenschow, D. H. and Spyers-Duran, P.: Measurement techniques: Air motion sensing, National Center for Atmospheric Research, Bulletin, 1989.

https://doi.org/10.5194/essd-2026-134
Preprint. Discussion started: 20 April 2026

340 Sasse, R. and Argrow, B.: CFD-Assisted Calibration of a Multi-Hole Probe for a Small UAS, AIAA SciTech 2022 Forum, 2400,

Sasse, R., Calmer, R., Quint, D., de Boer, G., Argrow, B., Frew, E. W., Wussow, M., Rhodes, M., Gómez-Faulk, C., and Ritsch, M.: Uncertainty Estimation for Small-UAS Wind Measurements in Calm and Dynamic Environments, 104th Annual AMS Meeting 2024, 431970,

345 Sasse, R. B.: A Comprehensive Approach to Aircraft Wind Measurement: Instrument Calibration and Sensor Fusion for Uncertainty Bounded Wind Estimation, University of Colorado at Boulder, 2025.